

Semiclassical Real-Time Nuclear-Electronic Orbital Dynamics for Molecular Polaritons: Unified Theory of Electronic and Vibrational Strong Couplings

Tao E. Li,^{*} Zhen Tao, and Sharon Hammes-Schiffer^{*}

Department of Chemistry, Yale University, New Haven, Connecticut, 06520, USA

E-mail: tao.li@yale.edu; sharon.hammes-schiffer@yale.edu

Abstract

Molecular polaritons have become an emerging platform for remotely controlling molecular properties through strong light-matter interactions. Herein, a semiclassical approach is developed for describing molecular polaritons by self-consistently propagating the real-time dynamics of classical cavity modes and a quantum molecular subsystem described by the nuclear-electronic orbital (NEO) method, where electrons and specified nuclei are treated quantum mechanically on the same level. This semiclassical real-time NEO approach provides a unified description of electronic and vibrational strong couplings and describes the impact of the cavity on coupled nuclear-electronic dynamics while including nuclear quantum effects. For a single *o*-hydroxybenzaldehyde molecule under electronic strong coupling, this approach shows that the cavity suppression of excited state intramolecular proton transfer is influenced not only by the polaritonic potential energy surface but also by the timescale of the chemical reaction. This work provides the foundation for exploring collective strong coupling in nuclear-electronic quantum dynamical systems within optical cavities.

1. Introduction

Molecular polaritons, hybrid light-matter states stemming from strong light-matter interactions,¹⁻⁶ have attracted extensive experimental and theoretical attention due to the potential for modifying molecular properties. Examples of applications include controlling energy transfer,⁷⁻⁹ promoting electronic conductivity,¹⁰ and modifying photochemical¹¹ and thermal¹²⁻¹⁴ chemical reaction rates. Molecular polaritons can form in different experimental setups, ranging from optical cavities,¹⁵ in which a large ensemble of molecules is coupled to a confined photon mode, to plasmonic nanocavities,¹⁶ in which a small number of molecules, possibly a single molecule,¹⁷ is coupled to a plasmonic mode. Depending on the frequency domain of the optical or plasmonic cavity mode, molecular polaritons can be mainly categorized as exciton-polaritons^{15,18} or the recently discovered vibrational polaritons,^{19,20} where a molecular electronic or vibrational transition, respectively, is strongly coupled to a cavity mode.

In these electronic strong coupling (ESC) and vibrational strong coupling (VSC) domains, the intriguing experimental findings have been sparking intensive theoretical developments to enable the description of molecular polaritons.²¹⁻³⁴ Conventional quantum-optical theories of polaritons³⁵⁻³⁷ usually approximate the molecular electronic or vibrational transitions as two-level systems and the cavity mode as a harmonic oscillator. Thus, these approaches may fail to capture some important cavity effects of experimental interest, such as chemical bond formation and dissociation. During the past decade, theories of molecular polaritons have been expanded to include the molecular details^{21-30,34} and the cavity mode structure beyond a single harmonic oscillator.³¹⁻³³ For example, under ESC, quantum-electrodynamical density functional theory (QEDFT)^{21,22,38} extends time-dependent density functional theory (TDDFT),³⁹ an efficient electronic structure method for calculating electronic excited states, to describe a polaritonic potential energy surface. Under VSC, the recently developed classical cavity molecular dynamics (CavMD)^{26,40} approach treats the infrared cavity mode as an additional "nuclear" coordinate, and a fully classical simulation of the coupled cavity-nuclear

system has been shown to qualitatively capture nonequilibrium dynamics under collective VSC arising from an ensemble of molecules coupled to the infrared cavity. Other methods such as the exaction factorization⁴¹ and multiconfigurational time-dependent Hartree method (MCTDH)²⁷ also provide an accurate description of quantum effects under ESC or VSC. In addition to a fully quantum or classical treatment of the coupled cavity-molecular system, a variety of semiclassical treatments of the light-matter system⁴²⁻⁴⁸ have also been shown to have the potential to accurately predict many light-involved processes from weak coupling to ESC.

Here, we report a novel semiclassical approach for describing molecular polaritons in which the quantum dynamics of the coupled nuclear-electronic system are self-consistently coupled to classical cavity modes. This approach is based on the recently developed real-time nuclear-electronic orbital TDDFT (RT-NEO-TDDFT)⁴⁹ approach, where both electronic and nuclear densities are propagated in real time. In contrast to full multicomponent TDDFT formalisms,⁵⁰⁻⁵² typically only specified protons are treated quantum mechanically on the same level as all electrons. Including both electron-electron exchange-correlation and electron-proton correlation effects,⁵³⁻⁵⁶ the linear-response⁵⁷ and real-time⁴⁹ NEO-TDDFT approaches have been shown to produce reliable electronic and proton vibrational excited states.^{58,59} These NEO approaches also include vibrational anharmonicity and nuclear quantum effects such as zero-point energies and proton delocalization. Moreover, the RT-NEO-TDDFT approach⁴⁹ has also been shown to directly capture the nonequilibrium coupled nuclear-electronic quantum dynamics of processes such as excited state proton transfer. The semiclassical RT-NEO-TDDFT approach combines the classical motion of cavity modes with the RT-NEO-TDDFT dynamics of the molecular system and propagates the coupled dynamics self-consistently. We will show that this semiclassical approach not only captures the hallmark of ESC and VSC, namely the real-time Rabi oscillations and frequency-domain Rabi splittings, in a unified manner, but also provides a straightforward means for evaluating the cavity effect on coupled nuclear-electronic dynamics while including nuclear quantum

effects.

The main advantages of the semiclassical RT-NEO-TDDFT approach are the straightforward implementation, the capability to describe both the ESC and VSC domains simultaneously, and the potential scalability to collective strong coupling due to the use of classical cavity modes. Under ESC, although a semiclassical treatment of the coupled cavity-electronic system may not be as accurate as full quantum treatments such as QEDFT,^{21,22} other work such as the semiclassical initial value representation (SC-IVR) method^{60,61} has shown that treating electronic degrees of freedom as classical harmonic oscillators is valid for many scenarios. Due to the harmonic nature of cavity modes, which can be viewed as standing electromagnetic waves, a classical treatment is expected to be a good approximation. Moreover, even when the cavity modes are treated classically, some quantum effects of the cavity modes can be recovered by introducing multiple trajectories in conjunction with the semiclassical algorithm.^{43,62,63} Additionally, in the limit of high excitations of cavity modes, a classical treatment becomes exact, whereas a quantum treatment usually requires greater computational cost to describe highly excited states. Under VSC, compared with a fully classical treatment such as CavMD,²⁶ the inclusion of quantum protons is expected to be more reliable for probing ultrafast vibrational polariton spectroscopy. In the remainder of the paper, we introduce the fundamental theoretical concepts and central equations underlying our semiclassical approach and present illustrative examples. These applications include both a single HCN molecule under ESC or VSC and the nonequilibrium dynamics of excited state intramolecular proton transfer.

2. Theory

2.1. QED Hamiltonian under long-wave approximation

We start from a quantum-electrodynamical (QED) Hamiltonian for light-matter interactions:^{22,64,65}

$$\hat{H}_{\text{QED}} = \hat{H}_{\text{M}} + \hat{H}_{\text{F}}. \quad (1a)$$

Here, \hat{H}_{M} denotes the conventional Hamiltonian for a molecular system composed of nuclei and electrons. This Hamiltonian is the sum of the kinetic and potential energies:

$$\hat{H}_{\text{M}} = \sum_i \frac{\hat{\mathbf{p}}_i^2}{2m_i} + \hat{V}_{\text{Coul}}(\{\hat{\mathbf{r}}_i\}), \quad (1b)$$

where m_i , $\hat{\mathbf{p}}_i$, and $\hat{\mathbf{r}}_i$ denote the mass, momentum operator, and position operator, respectively, for the i -th particle (i.e., nucleus or electron), and $\hat{V}_{\text{Coul}}(\{\hat{\mathbf{r}}_i\})$ denotes the Coulombic interaction operator among all nuclei and electrons.

Under the long-wave approximation, the field-related Hamiltonian \hat{H}_{F} is expressed as

$$\hat{H}_{\text{F}} = \sum_{k,\lambda} \frac{1}{2} \hat{p}_{k,\lambda}^2 + \frac{1}{2} \omega_{k,\lambda}^2 \left(\hat{q}_{k,\lambda} + \frac{1}{\omega_{k,\lambda} \sqrt{\Omega \epsilon_0}} \hat{\boldsymbol{\mu}}_S \cdot \boldsymbol{\xi}_\lambda \right)^2. \quad (1c)$$

The cavity photon mode is characterized by the wave vector $k = |\mathbf{k}|$ and the polarization direction $\boldsymbol{\xi}_\lambda$, which represents a unit vector satisfying $\mathbf{k} \cdot \boldsymbol{\xi}_\lambda = 0$ (i.e., if the \mathbf{k} direction is z , then λ is x or y). This photon mode is linearly coupled to $\hat{\boldsymbol{\mu}}_S$, the total (electronic plus nuclear) dipole moment of the molecular system. Here $\hat{p}_{k,\lambda}$, $\hat{q}_{k,\lambda}$, and $\omega_{k,\lambda}$ denote the momentum operator, position operator, and frequency, respectively, of the cavity photon. Ω denotes the effective volume of the cavity, and ϵ_0 denotes the vacuum permittivity.

2.2. Semiclassical approximation

We are interested in the semiclassical limit, where the cavity photons are treated classically.

In this limit, the full QED Hamiltonian in Eq. (1) can be rewritten as

$$\hat{H} = \hat{H}_{\text{sc}} + \sum_{k,\lambda} \frac{1}{2} p_{k,\lambda}^2 + \frac{1}{2} \omega_{k,\lambda}^2 q_{k,\lambda}^2, \quad (2a)$$

where the semiclassical light-matter Hamiltonian is

$$\hat{H}_{\text{sc}} = \hat{H}_{\text{M}} + \sum_{k,\lambda} \varepsilon_{k,\lambda} q_{k,\lambda} \hat{\mu}_\lambda. \quad (2b)$$

Here, the light-matter coupling strength $\varepsilon_{k,\lambda}$ is defined as

$$\varepsilon_{k,\lambda} = \frac{\omega_{k,\lambda}}{\sqrt{\Omega \epsilon_0}} \quad (2c)$$

and $\hat{\mu}_\lambda \equiv \hat{\boldsymbol{\mu}}_S \cdot \boldsymbol{\xi}_\lambda$ denotes the total (electronic plus nuclear) molecular dipole operator projected onto the direction of $\boldsymbol{\xi}_\lambda$.

Within this semiclassical treatment, the self-dipole term (i.e., the term proportional to $\hat{\boldsymbol{\mu}}_S^2$) in Eq. (1c) has been disregarded on the basis of the previous finding that neglecting this term is valid from weak to strong coupling,^{31,66} although it can fail under ultrastrong coupling.^{66,67} There is no unique semiclassical treatment for the self-dipole term,⁶⁸ and identifying the optimal semiclassical form of this term in the ultrastrong coupling limit is beyond the scope of this manuscript.

Given the semiclassical Hamiltonian defined in Eq. (2), we propagate the electrons and specified nuclei, typically protons, quantum mechanically and propagate the cavity photons classically. In particular, we propagate the dynamics of both electrons and quantum nuclei with the time-dependent Schrödinger equation:

$$i\hbar \frac{\partial}{\partial t} \Psi(\mathbf{x}^e, \mathbf{x}^n; t) = \hat{H}_{\text{sc}}(\mathbf{x}^e, \mathbf{x}^n; t) \Psi(\mathbf{x}^e, \mathbf{x}^n; t), \quad (3)$$

where \mathbf{x}^e (or \mathbf{x}^n) denotes the collective spatial and spin coordinates of the electrons (or quantum protons), and the remaining heavy nuclei are assumed fixed. This approximation is valid when the timescale of interest is smaller than the timescale of heavy nuclear motions, which is usually larger than tens of fs. On the other hand, we evolve the cavity photons according to the classical equations of motion:

$$\dot{q}_{k,\lambda} = p_{k,\lambda}, \quad (4a)$$

$$\dot{p}_{k,\lambda} = -\omega_{k,\lambda}^2 q_{k,\lambda} - \varepsilon_{k,\lambda} \mu_\lambda - \gamma_c p_{k,\lambda}. \quad (4b)$$

Here, γ_c denotes the cavity loss rate, which is introduced here to represent the imperfectness of the cavity mirrors. In our simulations, we set the initial photon conditions as $q_{k,\lambda}(t = 0) = p_{k,\lambda}(t = 0) = 0$ and define $\mu_\lambda(t) = \langle \hat{\mu}_\lambda(t) \rangle - \langle \hat{\mu}_\lambda(t = 0) \rangle$, where $\langle \dots \rangle$ denotes the molecular expectation value, thereby setting the molecular dipole moment to zero at $t = 0$ and neglecting the effect of the permanent dipole moment on the cavity photons. This treatment is necessary to ensure that the cavity photons will not be excited at $t > 0$ without any external perturbation, i.e., a system starting in the ground state will always remain in the ground state in the absence of external perturbation; see Sec. Simulation Details for additional explanations.

2.3. Semiclassical RT-NEO approach

Within the framework of the real-time NEO approach,⁴⁹ the nuclear-electronic wavefunction has the following form:

$$\Psi(\mathbf{x}^e, \mathbf{x}^n; t) = \Psi(\mathbf{x}^e; t) \Psi(\mathbf{x}^n; t), \quad (5)$$

and the time-dependent Schrödinger equation can be propagated separately for the electronic and nuclear components. Here, we choose to propagate the von Neumann equations

$$i\hbar\frac{\partial}{\partial t}\mathbf{P}^e(t) = \left[\mathbf{F}^e(t) + \sum_{k,\lambda} \varepsilon_{k,\lambda} q_{k,\lambda}(t) \hat{\mu}_\lambda^e, \mathbf{P}^e(t) \right] \quad (6a)$$

$$i\hbar\frac{\partial}{\partial t}\mathbf{P}^n(t) = \left[\mathbf{F}^n(t) + \sum_{k,\lambda} \varepsilon_{k,\lambda} q_{k,\lambda}(t) \hat{\mu}_\lambda^n, \mathbf{P}^n(t) \right] \quad (6b)$$

in the orthogonal atomic orbital basis. The density matrices are defined as $\mathbf{P}^e = \mathbf{C}^e\mathbf{C}^{e\dagger}$ and $\mathbf{P}^n = \mathbf{C}^n\mathbf{C}^{n\dagger}$, where $\mathbf{C}^e(t)$ (or $\mathbf{C}^n(t)$) denotes the coefficient vector of the electronic (or nuclear) wavefunction in the orthogonal atomic orbital basis. $\hat{\mu}_\lambda^e = -|e|\sum_i \hat{r}_{i\lambda}^e$ and $\hat{\mu}_\lambda^n = |e|\sum_j Z_j \hat{r}_{j\lambda}^n$ denote the electronic and nuclear components of the molecular dipole moment, where e , $\hat{r}_{i\lambda}^e$, Z_j , and $\hat{r}_{j\lambda}^n$ denote the electronic charge, the $\lambda = x, y$, or z component of the electronic position operator, the nuclear charge, and the λ component of the nuclear position operator, respectively. $\mathbf{F}^e(t)$ (or $\mathbf{F}^n(t)$) denotes the Kohn–Sham matrix for the electrons (or nuclei) in the orthogonal atomic orbital basis:

$$\mathbf{F}^e(t) = \mathbf{H}_{\text{core}}^e + \mathbf{J}^{ee}(\mathbf{P}^e(t)) + \mathbf{V}_{\text{xc}}^e(\mathbf{P}^e(t)) - \mathbf{J}^{\text{en}}(\mathbf{P}^n(t)) - \mathbf{V}_c^{\text{en}}(\mathbf{P}^e(t), \mathbf{P}^n(t)) + \mathbf{V}_{\text{ext}}^e(t) \quad (7a)$$

$$\mathbf{F}^n(t) = \mathbf{H}_{\text{core}}^n + \mathbf{J}^{\text{nn}}(\mathbf{P}^n(t)) + \mathbf{V}_{\text{xc}}^n(\mathbf{P}^n(t)) - \mathbf{J}^{\text{ne}}(\mathbf{P}^e(t)) - \mathbf{V}_c^{\text{ne}}(\mathbf{P}^n(t), \mathbf{P}^e(t)) + \mathbf{V}_{\text{ext}}^n(t) \quad (7b)$$

Here, $\mathbf{H}_{\text{core}}^{e(n)}$ denotes the core Hamiltonian that includes the kinetic energy and the Coulomb interaction of the electrons or quantum nuclei with the classical nuclei; $\mathbf{J}^{ee(\text{nn})}$ denotes the Coulomb interactions for the electrons or quantum nuclei; $\mathbf{V}_{\text{xc}}^{e(n)}$ denotes the exchange–correlation potential for the electrons or quantum nuclei; $\mathbf{J}^{\text{ne}(\text{en})}$ denotes the Coulomb interaction between the electrons and quantum nuclei; $\mathbf{V}_c^{\text{ne}(\text{en})}$ denotes the correlation potential between the electrons and quantum nuclei; $\mathbf{V}_{\text{ext}}^{e(n)}(t)$ denotes the time-dependent external potential such as the light–matter coupling with the external pulse. Note that the classical nuclei are treated as fixed classical point charges and do not contribute to the change in the molecular dipole moment relative to $t = 0$.

Eqs. (4) and (6) form the working equations of the semiclassical RT-NEO approach of QED. We will use two molecular examples to illustrate the advantages and capabilities of this approach. For a single HCN molecule with all electrons and the proton treated quantum mechanically, we show that our semiclassical RT-NEO-TDDFT calculation captures the real-time Rabi oscillations as well as the frequency-domain Rabi splitting under both ESC and VSC. For the *o*-hydroxybenzaldehyde (oHBA) molecule under ESC, with all electrons and the transferring proton treated quantum mechanically, our approach reveals the impact of the cavity on excited-state proton transfer dynamics. In the next section, we will provide additional simulation details.

3. Simulation Details

The semiclassical RT-NEO-TDDFT approach has been implemented in a developer version of Q-Chem.⁶⁹ This approach entails propagation of Eqs. (4) and (6). We propagate the quantum molecular subsystem with a modified-midpoint unitary transform time-propagation scheme algorithm.^{70,71} An additional predictor-corrector procedure⁷² is used to control the growth of numerical error during time propagation. The velocity Verlet algorithm is used to propagate the classical cavity mode. The classical nuclei of the molecule are fixed at the specified geometry. The outside cavity parameters are similar to those used in Ref.⁴⁹ The input files and plotting scripts are available at Github (<https://github.com/TaoELi/semiclassical-rt-neo>).

The initial conditions for propagating Eqs. (4) and (6) are chosen to be the SCF ground state for the electronic and nuclear density matrices, $\mathbf{P}^{\text{e,n}}(t=0)$, and $q_{k,\lambda}(t=0) = p_{k,\lambda}(t=0) = 0$ for the classical cavity mode. In Eq. (4), the evaluation of μ_λ requires additional explanation. As mentioned above, we define $\mu_\lambda(t) = \langle \hat{\mu}_\lambda(t) \rangle - \langle \hat{\mu}_\lambda(t=0) \rangle$, thereby neglecting the effect of the permanent dipole moment on the cavity photons and ensuring that the cavity photons will not be excited at $t > 0$ without any external perturbation. If we use an

alternative strategy, in which $\mu_\lambda(t) = \langle \hat{\mu}_\lambda(t) \rangle$ (i.e., we consider the effect of the permanent dipole moment) and also set $q_{k,\lambda}(t=0)$ in a manner that satisfies $\dot{p}_{k,\lambda}(t=0) = 0$ in Eq. (4), we can also ensure that the ground state will remain unchanged at $t > 0$ in the absence of an external perturbation. This alternative strategy, which may contain an initial condition of $q_{k,\lambda}(t=0) \neq 0$ when the molecular permanent dipole is nonzero, can be understood physically in terms of a polarized photon field^{66,73} but is practically equivalent to our default treatment.

For the DFT calculations, we use the B3LYP functional^{74–76} for electron–electron exchange–correlation and the epc17-2 functional^{54,55} for electron–proton correlation. When calculating the SCF ground state, a tight convergence criterion is needed to reduce the computational error in the real-time simulation (see SI for the input files). A time step of $\Delta t = 0.04$ a.u. is used for the real-time simulation.

For the HCN simulations, we use the cc-pVDZ electronic basis set⁷⁷ and an even-tempered *8s8p8d* protonic basis set⁵⁴ with exponents ranging from $2\sqrt{2}$ to 32. Outside the cavity, at $t = 0$, we apply a delta pulse to both the electronic and protonic Fock matrices, which can be expressed as $\mathbf{F}'^{e,n} + \mathbf{E} \cdot \boldsymbol{\mu}'^{e,n}$. Here, $\mathbf{E} = (E_0, E_0, E_0)$ with $E_0 = 0.01$ a.u., and $\mathbf{F}'^{e,n}$ and $\boldsymbol{\mu}'^{e,n}$ denote the electronic or protonic Fock matrix and dipole moment vector matrix (in three dimensions) evaluated in the nonorthogonal atomic orbital basis, which are labeled with a prime superscript to distinguish from Eq. (6), where the matrices are expressed in the orthogonal atomic orbital basis. Inside the cavity, we apply a delta pulse to the cavity mode (instead of the molecule) at $t = 0$: $q_c = q_c(t=0) + \Delta q_c$, where $\Delta q_c = 0.001$ a.u. under ESC and $\Delta q_c = 0.3$ a.u. under VSC to increase the signal of the protonic dipole moment and reduce the relative numerical error.

We then calculate the power spectrum of the real-time dipole signal by a Fourier transformation. Note that since we have only propagated a short range of time (50 fs), a direct Fourier transformation does not provide sufficient resolution in the frequency domain. In order to obtain enough resolution, following Refs.^{70,78}, we take the Padé approximation of

the Fourier transform and calculate the power spectrum as follows:

$$P_e(\omega) = \sum_{i=x,y,z} |\mathcal{F}[\mu_i^e(t)e^{-\gamma t}]|. \quad (8)$$

Because the dipole signal calculated from real-time time-dependent electronic structure theory does not contain any damping, a small damping term $e^{-\gamma t}$ is used (with $\gamma = 10^{-5}$ a.u.) to give an artificial linewidth of 1.7×10^{-3} eV = 13.8 cm⁻¹ to all of the peaks in the spectra.

For the oHBA simulations, the cc-pVDZ electronic basis set is used in conjunction with a small *1s1p* protonic basis set with an exponent of 4 to provide a qualitative description of the proton transfer reaction. The proton position is evaluated by $\text{Tr}(\mathbf{r}'^n \mathbf{P}'^n)$, where \mathbf{r}'^n and \mathbf{P}'^n denote the protonic position matrix and density matrix evaluated in the nonorthogonal atomic orbital basis. At $t = 0$, we model the $S_0 \rightarrow S_1$ transition by enforcing a HOMO to LUMO transition in the electronic density matrix. In order to simulate proton transfer, we have added three additional proton basis function centers; see SI for the corresponding coordinates.

4. Results

4.1. Electronic strong coupling

Our first example is a single HCN molecule oriented along the z axis. Starting from the nuclear-electronic self-consistent field (SCF) ground state, this molecule is perturbed by a weak delta pulse at $t = 0$. Fig. 1a shows the real-time dynamics of the electronic dipole moment in the z direction, $\mu_z^e(t) \equiv \langle \hat{\mu}_z^e(t) \rangle - \langle \hat{\mu}_z^e(t = 0) \rangle$, outside the cavity for 50 fs. Fig. 1b shows the corresponding electronic power spectrum $P_e(\omega)$ of the HCN molecule (solid blue line). In order to check the validity of the real-time simulation, we also plot the electronic transitions calculated from linear-response NEO-TDDFT method (dashed black line). The relative heights of the linear-response peaks represent the corresponding oscillator strengths,

where the maximum value is normalized to unity. The excellent agreement between the real-time and linear-response peaks (with a difference smaller than 10^{-3} eV) confirms the numerical stability of our real-time simulation.

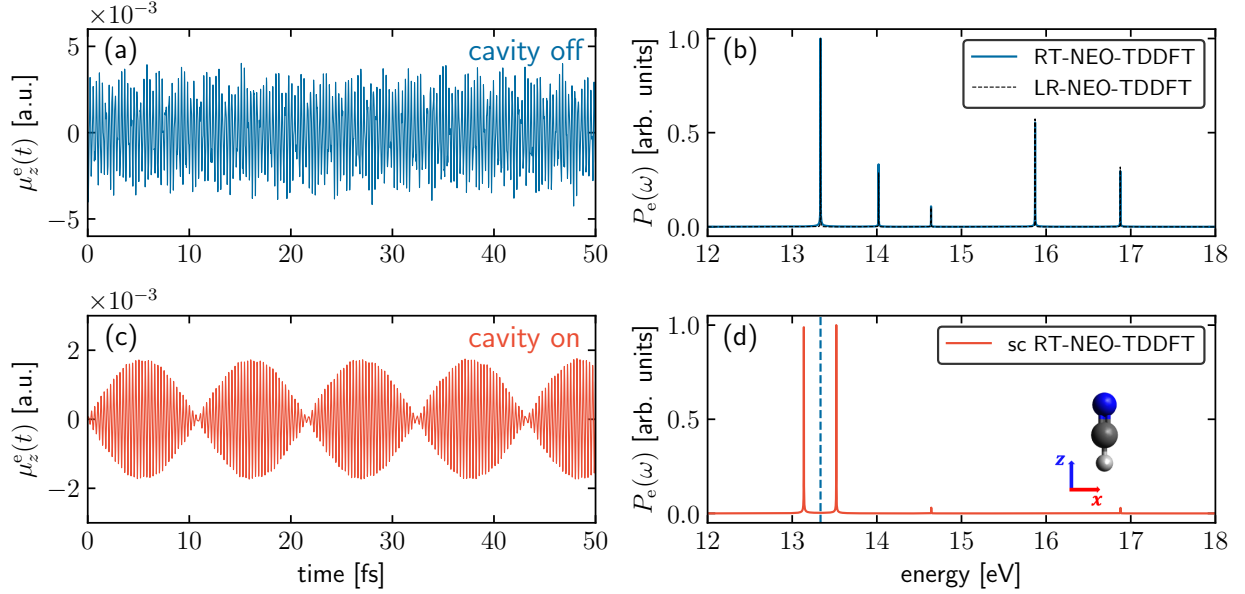


Figure 1: (a) Real-time NEO-TDDFT dynamics of the z -component of the HCN electronic dipole moment, $\mu_z^e(t)$, in free space when the molecule is perturbed by a delta pulse. (b) Corresponding power spectrum, $P_e(\omega)$, of the real-time dipole signal in (a) (blue line) as well as the linear-response NEO-TDDFT excited electronic state transitions (dashed black line). The real-time and linear-response spectra are virtually indistinguishable. (c) Semiclassical RT-NEO-TDDFT dynamics of $\mu_z^e(t)$ when the HCN molecule is resonantly coupled to a z -polarized cavity mode with frequency $\omega_c = 13.334$ eV, coupling strength $\varepsilon = 4 \times 10^{-3}$ a.u., and no loss, and the cavity mode is perturbed by a delta pulse at $t = 0$. (d) Corresponding power spectrum, $P_e(\omega)$, of the real-time dipole signal in (c). The geometry and orientation of the HCN molecule are also depicted in (d). The vertical dashed blue line denotes the cavity mode frequency, which is at resonance with an electronic transition in (b). Note that Rabi oscillations are observed in real time (c), and an UP and LP pair is formed in the frequency domain (d). All peaks in these spectra have an artificial linewidth of 1.7×10^{-3} eV because a small damping term $e^{-\gamma t}$ with $\gamma = 10^{-5}$ a.u. is used to process the real-time signals.

Next we simulate the real-time dynamics inside the cavity with a z -polarized lossless cavity mode at resonance with the strongest electronic peak in Fig. 1b ($\omega_c = 13.334$ eV) and the coupling strength set to $\varepsilon = 4 \times 10^{-3}$ a.u. The choice of a z -polarized cavity mode is to align with the largest transition dipole component among the three dimensions, where the geometry and orientation of the HCN molecule are depicted in Fig. 1d. Fig. 1c shows the

dynamics of $\mu_z^e(t)$ when the cavity mode (not the molecule) is perturbed by a weak delta pulse at $t = 0$. In this case, real-time Rabi oscillations are observed due to the coherent energy exchange between the cavity mode and the molecular electronic transition. In the frequency domain, as shown in Fig. 1d, the original electronic peak at 13.334 eV (vertical dashed blue line) is split into two peaks, known as the lower polariton (LP) and the upper polariton (UP). These two polaritons are separated by a Rabi splitting of $\Omega_R = 0.384$ eV. The other electronic peaks in Fig. 1b are not significantly excited in Fig. 1d because the cavity mode frequency is far from these off-resonant electronic peaks, and therefore the excited cavity mode transfers only a small amount of energy to these electronic transitions. Figure S1 in the SI illustrates how the polaritonic spectrum depends on the cavity loss and light-matter coupling strength.

4.2. Vibrational strong coupling

In addition to the ESC domain, one important advantage of the semiclassical RT-NEO approach is the capability of treating the VSC domain. Again, we use the HCN molecule oriented along the x axis as an example. Outside the cavity, Figs. 2a,b show the dynamics of the x -component of the nuclear dipole moment, $\mu_x^n(t)$ in the time domain and the corresponding power spectrum in the frequency domain. In Fig. 2b, the linear-response NEO-TDDFT peaks (dashed black line) are shown to be in very good agreement with the real-time NEO-TDDFT peaks. Specifically, the peak difference is 1 cm^{-1} for the HCN bending modes (left) and 12 cm^{-1} for the HCN stretching mode (right) with nearly identical relative oscillator strengths between the two peaks.

Next an x -polarized lossless cavity mode is resonantly coupled to the HCN bending mode with cavity frequency $\omega_c = 2803 \text{ cm}^{-1}$ and coupling strength $\varepsilon = 4 \times 10^{-4}$ a.u. For the HCN geometry oriented along the z -direction, which is shown in Fig. 2d, the doubly degenerate bending mode oscillates in the xy plane. Fig. 2c shows the dynamics of $\mu_x^n(t)$ for 50 fs after a weak perturbation of the cavity mode (not the molecule) at $t = 0$. As the proton evolves

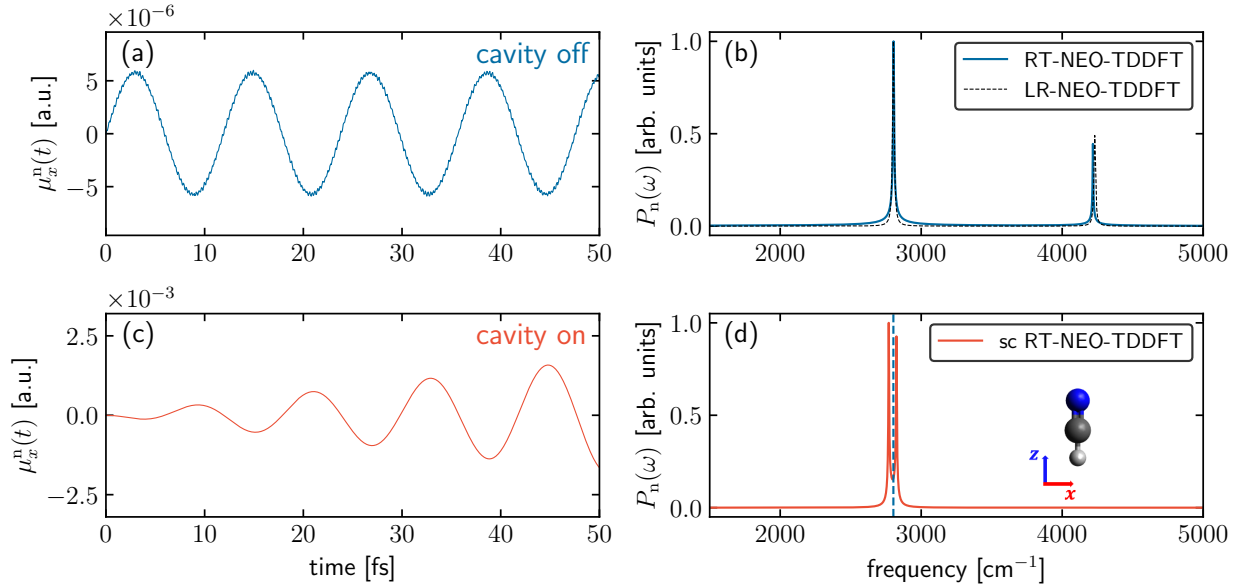


Figure 2: (a) Real-time NEO-TDDFT dynamics of the x -component of the HCN nuclear dipole moment, $\mu_x^n(t)$, in free space when the molecule is perturbed by a delta pulse. (b) Corresponding power spectrum, $P_n(\omega)$, of the dipole signal in (a) (blue line) as well as the linear-response NEO-TDDFT excited vibrational state transitions (dashed black line). The real-time and linear-response spectra are virtually indistinguishable. (c) Semiclassical RT-NEO-TDDFT dynamics of $\mu_x^n(t)$ when the HCN molecule is resonantly coupled to an x -polarized cavity mode with frequency $\omega_c = 2803 \text{ cm}^{-1}$, coupling strength $\varepsilon = 4 \times 10^{-4} \text{ a.u.}$, and no loss, and the cavity mode is perturbed by a delta pulse at $t = 0$. (d) Corresponding power spectrum, $P_n(\omega)$, of the real-time dipole signal in (c). The vertical dashed blue line denotes the cavity mode frequency, which is at resonance with the lowest vibrational transition in (b). All peaks in these spectra have an artificial linewidth of $1.7 \times 10^{-3} \text{ eV}$ (13.8 cm^{-1}) because a small damping term $e^{-\gamma t}$ with $\gamma = 10^{-5} \text{ a.u.}$ is used to process the real-time signals.

much more slowly than the electrons, within 50 fs the molecule has not finished a period of Rabi oscillation, in contrast to the ESC case. In the frequency domain, however, as shown in Fig. 2d, the observation of a pair of polaritons with a Rabi splitting of $\Omega_R = 55 \text{ cm}^{-1}$ implies VSC.

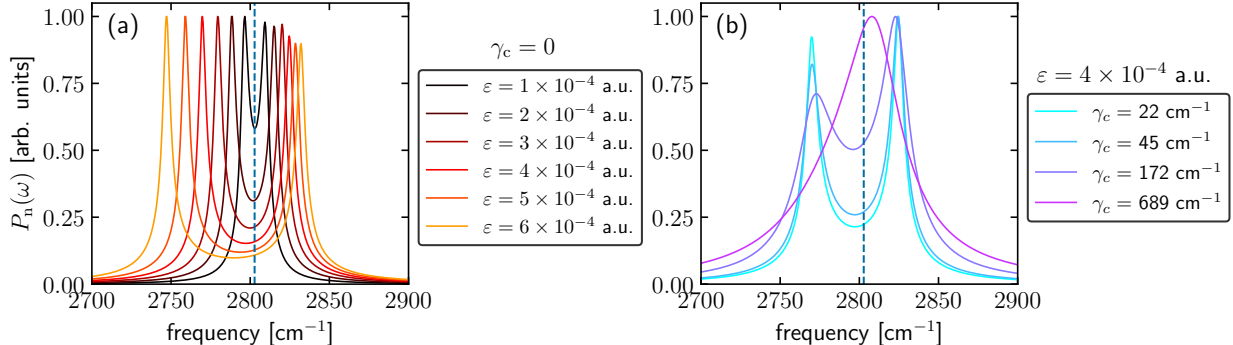


Figure 3: Power spectrum, $P_n(\omega)$, of the HCN nuclear dipole moment when the HCN bending modes are resonantly coupled to the x -polarized cavity with frequency $\omega_c = 2803 \text{ cm}^{-1}$ (vertical dashed blue lines). (a) No cavity loss and the light-matter coupling strength ranges from $\varepsilon = 1 \times 10^{-4} \text{ a.u.}$ (black line) to $6 \times 10^{-4} \text{ a.u.}$ (orange line). (b) The cavity loss ranges from $\gamma_c = 22 \text{ cm}^{-1}$ (cyan line) to 689 cm^{-1} (purple line) with the light-matter coupling strength set to $\varepsilon = 4 \times 10^{-4} \text{ a.u.}$ Increasing the cavity loss transforms the system from strong coupling (with a peak splitting) to weak coupling (with no peak splitting). All other simulation details are the same as for Fig. 2d. The molecular peaks have an artificial linewidth of 13.8 cm^{-1} because of the small damping term used during signal processing. In part (b), the linewidths only partially arise from the signal processing and mostly originate from the coupling to the lossy cavity.

In Fig. 3, we analyze the dependence of the polaritonic spectrum on the coupling strength and cavity loss for the VSC case. With all other parameters the same as in Fig. 2d, Fig. 3a shows the polariton spectrum when the coupling strength between the lossless cavity and the molecule is tuned from $\varepsilon = 1 \times 10^{-4} \text{ a.u.}$ (black line) to $6 \times 10^{-4} \text{ a.u.}$ (orange line). As the coupling strength is increased, the Rabi splitting increases asymmetrically. Such asymmetric behavior, where the LP shifts more than the UP, is not observed for HCN under ESC (see SI Fig. S1), most likely because the excitation is significantly higher. However, this asymmetry is also observed under ESC for the proton transfer system discussed below, which is also a relatively low-frequency excitation, as well as in a previous QED electronic

structure calculation.⁷⁹ The origin of our asymmetry, in which the LP shifts more than the UP, is currently unclear. In our treatment, the self-dipole term in the QED Hamiltonian has been neglected. Although Ref.⁷⁹ concludes that similar asymmetry arises from the inclusion of the self-dipole term in the QED Hamiltonian, Ref.²⁶ suggests that including the self-dipole term would cause an opposite asymmetry, where the UP shifts more than the LP. The latter asymmetry agrees with the standard Hopfield model,⁸⁰ in which the A^2 term is included in the QED Hamiltonian. Thus, this issue warrants further investigation.

When the coupling strength is fixed as $\varepsilon = 4 \times 10^{-4}$ a.u., Fig. 3b shows the polariton spectrum when the cavity loss rate increases from $\gamma_c = 22 \text{ cm}^{-1}$ (cyan line) to 689 cm^{-1} (purple line). When the cavity loss increases, the polariton linewidths increase until the Rabi splitting ($\Omega_R = 55 \text{ cm}^{-1}$) disappears, illustrating a transition from strong coupling to weak coupling when the cavity loss increases. In Fig. 3a, the linewidths arise from the signal processing, whereas in Fig. 3b, the linewidths arise partially from the signal processing but mainly from the coupling to the lossy cavity.

4.3. Proton transfer dynamics under electronic strong coupling

Beyond simulating real-time Rabi oscillations and the frequency-domain Rabi splitting, our semiclassical RT-NEO-TDDFT approach also provides a straightforward means to probe nonequilibrium coupled nuclear-electronic dynamics under ESC or VSC conditions in a cavity. As an example, we consider the ESC effect on excited state intramolecular proton transfer (ESIPT)^{81,82} for a single oHBA molecule inside the cavity. Unless otherwise specified, all of these calculations are performed for the restricted excited state geometry, which was obtained by optimizing the geometry in the electronically excited state with the distance between the proton and the donor oxygen constrained to its ground state value,⁸² as depicted in the inset of Fig. 4a.

Outside the cavity, photoexcitation induces the proton to transfer from the donor oxygen atom (O_D) to the acceptor oxygen atom (O_A). To characterize this proton transfer reaction,

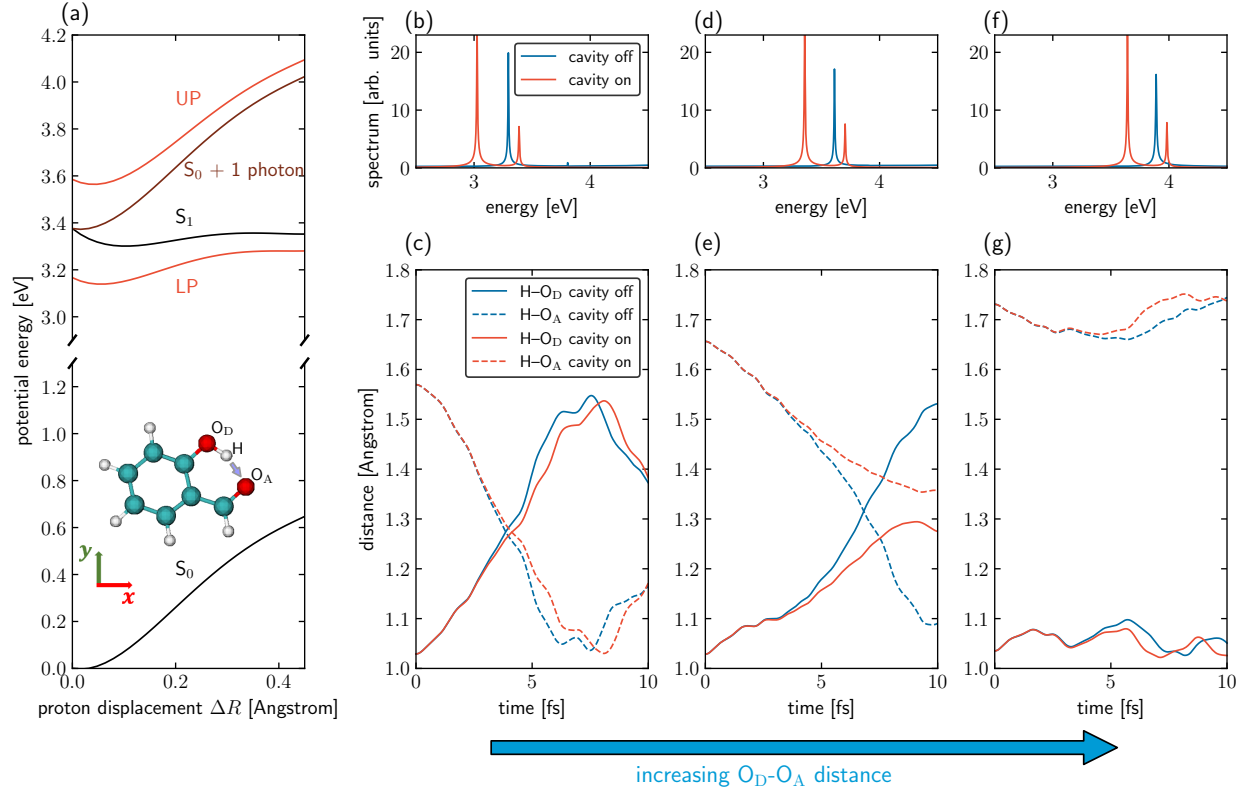


Figure 4: Excited state intramolecular proton transfer dynamics for an oHBA molecule under ESC. (a) Polaritonic potential energy surfaces as a function of proton displacement (ΔR) for the oHBA molecule shown in the inset. The S_0 and S_1 states (black lines) are calculated by conventional LR-TDDFT. The minimum on S_1 corresponding to the proton bonded to O_A is $\Delta R = 0.45$ Å. A pair of polaritonic states form (UP and LP, red lines) when the S_1 state is near resonance with the S_0 state dressed with a singly excited cavity photon (brown line); see Eq. (9) for the effective Hamiltonian. (b) The corresponding power spectrum of the electronic dipole moment outside the cavity (blue line) or inside a lossless cavity (red line) when a y -polarized cavity mode is at resonance with the $S_0 \rightarrow S_1$ transition (blue peak at 3.295 eV) with $\varepsilon = 4 \times 10^{-3}$ a.u. (c) The corresponding excited-state intramolecular proton transfer dynamics outside (blue lines) or inside (red lines) the cavity. Solid (or dashed) lines denote the distance between the expectation value of the proton position and the donor (or acceptor) oxygen atom. (d,e) and (f,g) Two sets of spectra and proton transfer dynamics outside or inside the cavity when the distance between the oxygen atoms is increased. In Figs. (c), (e), and (g), the distance between the O_D and O_A atoms is 2.51 Å, 2.57 Å, and 2.64 Å, respectively. When the proton transfer timescale (indicated by the crossing point of the red and blue lines) is smaller than the Rabi oscillation timescale (~ 11 fs), negligible cavity suppression of proton transfer is observed, as shown in (c), whereas increasing the proton transfer timescale while retaining a similar Rabi splitting leads to much greater cavity suppression of proton transfer, as shown in (d) and (e).

Fig. 4a shows the LR-TDDFT potential energy surface for the S_0 and S_1 states (black lines) when the proton is displaced by ΔR from its initial position along the vector connecting this initial position and O_A . Intramolecular proton transfer is only facile on the S_1 excited-state surface because for the S_1 surface, the energy at $\Delta R = 0$ is greater than the energies over the range $0 < \Delta R < 0.45 \text{ \AA}$. Note that this figure depicts only a slice of the molecular multidimensional potential energy surface along ΔR and may not represent the reaction path followed by the proton.

Next we consider the case when the $S_0 \rightarrow S_1$ electronic transition at $\Delta R = 0$ is resonantly coupled to a cavity mode. In the singly excited manifold, at each proton displacement ΔR , the bare S_1 state is coupled to the S_0 state dressed by an excited cavity mode (brown line). Quantitatively, we can express the effective light-matter Hamiltonian in the singly excited manifold as

$$\begin{pmatrix} E_{S_1}(\Delta R) & -\boldsymbol{\mu}_{S_0 \rightarrow S_1}(\Delta R) \cdot \boldsymbol{\mathcal{E}} \\ -\boldsymbol{\mu}_{S_0 \rightarrow S_1}(\Delta R) \cdot \boldsymbol{\mathcal{E}} & E_{S_0}(\Delta R) + E_{\text{ph}} \end{pmatrix}. \quad (9)$$

Here, $E_{S_1}(\Delta R)$ and $E_{S_0}(\Delta R)$ denote the bare S_1 and S_0 state energies outside the cavity, $\boldsymbol{\mu}_{S_0 \rightarrow S_1}(\Delta R)$ denotes the transition dipole moment vector between these two states, and $\boldsymbol{\mathcal{E}}$ denotes the effective electric field vector inside the cavity. Setting $\boldsymbol{\mathcal{E}} = (0, 0.3 \text{ a.u.}, 0)$, we diagonalize the Hamiltonian in Eq. (9) at different values of ΔR and obtain the eigenstates, which correspond to the LP and UP states (red lines). Similar to a previous theoretical study⁸³ of the ESC effect on photoisomerization, these calculations suggest that the proton transfer dynamics will be suppressed on both the LP and the UP potential energy surfaces compared to the original S_1 channel.

Analogous to the procedure applied to HCN above, we used the RT-NEO-TDDFT method to compute the power spectra when all electrons and the transferring proton are treated quantum mechanically. Fig. 4b shows the spectra outside the cavity (blue line) and inside a lossless cavity (red line) when the y -polarized cavity mode is resonantly coupled to the $S_0 \rightarrow S_1$ electronic transition (blue peak at 3.295 eV) with $\varepsilon = 4 \times 10^{-3} \text{ a.u.}$ Inside the

cavity, a pair of polaritons forms with the Rabi splitting $\Omega_R = 0.361$ eV (red line). Note that when computing the spectra, a very weak pulse is used to excite the system, and therefore the molecule remains predominantly in the ground vibronic state and proton transfer does not occur.

To simulate photoinduced ESIPT in this molecule, we model the $S_0 \rightarrow S_1$ electronic transition by exciting the electronic density matrix from the highest occupied molecular orbital (HOMO) to the lowest unoccupied molecular orbital (LUMO) at $t = 0$. Inside the cavity, such an initial condition corresponds to an approximately equal excitation of the LP and UP, which could be realized experimentally by sending a wide-band pulse to excite the molecular system. The proton transfer process is monitored by plotting the distance between the proton and O_D and the distance between the proton and O_A , where the proton moves away from the donor and toward the acceptor, as shown in 4c. These distances are computed with the expectation value of the proton position. The proton transfer time is defined as the time at which these two distances are the same. Outside the cavity (blue lines), the proton transfers at ~ 4.2 fs and starts returning to O_D at $t \approx 8$ fs, similar to previous RT-NEO-TDDFT studies of this molecule in free space.⁴⁹

Inside the cavity (red lines), the proton dynamics is only slightly suppressed. As the Rabi splitting here is similar to the splitting between the polaritonic potential energy surfaces ($\Delta R = 0$ in Fig. 4a), such a negligible cavity effect appears to conflict with previous theoretical predictions.⁸³ We hypothesized that this negligible effect was due to the faster timescale of proton transfer (~ 4 fs) compared to the Rabi oscillation timescale (11.5 fs based on $\Omega_R = 0.361$ eV). In this case, proton transfer itself effectively serves as a strong lossy channel that breaks down strong coupling. In other words, the energy transfer dynamics between the proton and the cavity mode, which is characterized by the Rabi splitting, is slower than the proton transfer dynamics, preventing the cavity from significantly influencing the proton transfer dynamics. According to this hypothesis, if the proton transfer dynamics is slowed down while the Rabi splitting remains the same, we expect to observe a stronger

cavity suppression of proton transfer.

To test this hypothesis, we increase the distance between the O_D and O_A atoms for the fixed geometry used in these simulations. As shown in Figs. 4d,e, outside the cavity (blue lines), the proton transfer time increases to 7 fs and starts returning at 10 fs. When the lossless y -polarized cavity is again resonantly coupled to the $S_0 \rightarrow S_1$ transition (blue peak at 3.611 eV) with $\varepsilon = 4 \times 10^{-3}$ a.u., the Rabi splitting ($\Omega_R = 0.348$ eV, corresponding to 11.9 fs) is similar to that in Fig. 4b, but the proton transfer dynamics (red lines) is greatly suppressed compared with that outside the cavity (blue lines). Comparing Fig. 4e to Fig. 4c, we observe a much stronger cavity suppression of proton transfer when the proton transfer timescale is extended while the Rabi splitting remains similar, thus confirming our above hypothesis. For Fig. 4e, the corresponding electronic density (the green isosurface) and protonic density (the blue isosurface) at time $t = 0$ fs and 9.7 fs are plotted in the table of contents (TOC) figure. When the distance between the O_D and O_A atoms is further increased, as shown in Figs. 4f,g, proton transfer does not occur either inside or outside the cavity.

For the nuclear geometries used to generate the data in Fig. 4c or 4e, we have also observed that the cavity suppression effect becomes more substantial when the light-matter coupling strength ε is increased (see SI Fig. S2). This finding is consistent with our above hypothesis because increasing ε can lead to a smaller Rabi oscillation timescale due to a larger Rabi splitting. In this case, the proton transfer timescale becomes more similar to the Rabi oscillation timescale, which, according to our hypothesis, implies a larger cavity suppression effect for proton transfer. Our hypothesis is also consistent with the observation that adding a cavity lifetime of 10 fs, which is slower than the proton transfer lifetime, does not alter the proton transfer dynamics (see SI Fig. S3).

A more realistic photoinduced ESIPT can be simulated by using an external Gaussian pulse to excite the molecular subsystem (not the cavity mode), in contrast to Fig. 4, where the proton transfer is triggered via a HOMO to LUMO transition at $t = 0$. Analogous

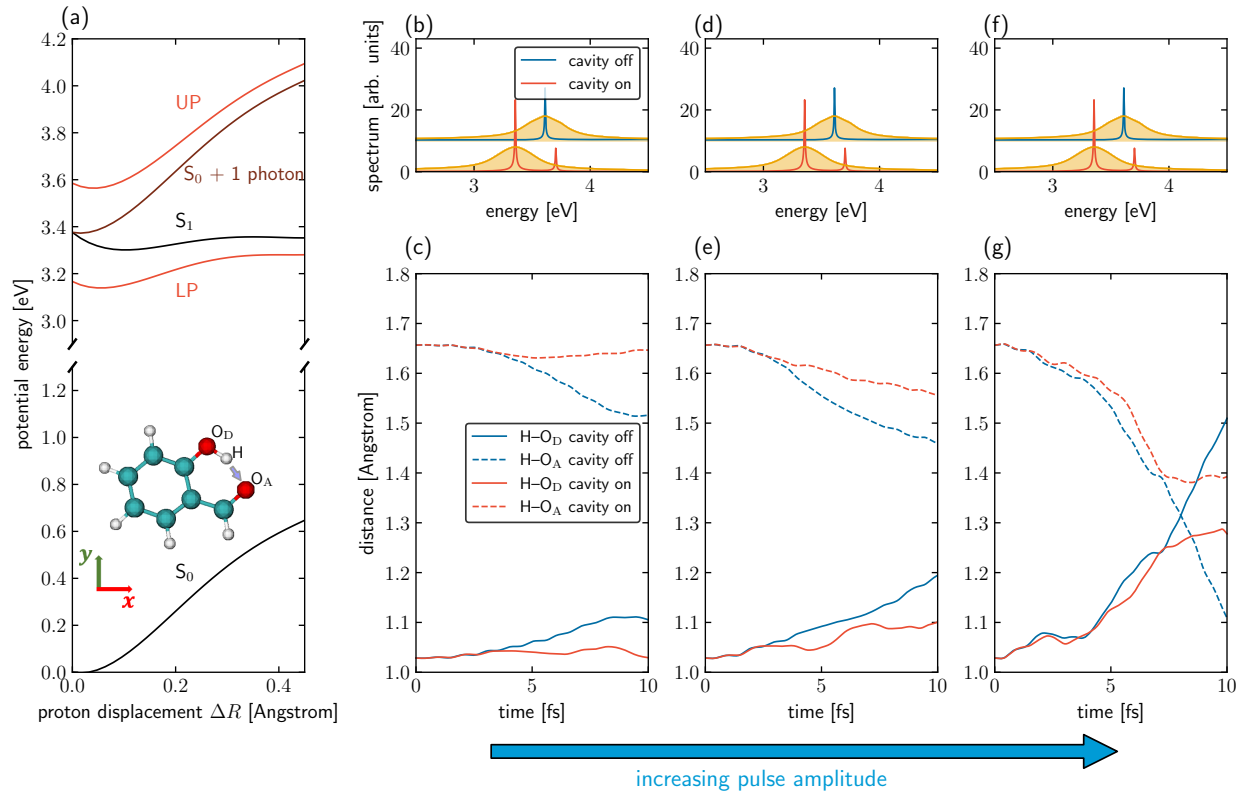


Figure 5: Excited state intramolecular proton transfer dynamics for an oHBA molecule under an external pulse excitation. Part (a) is identical to Fig. 4a. For (b)-(g), the oHBA geometry is fixed to the same geometry as that used in Figs. 4(d,e), and therefore the spectra in (b), (d), and (f) are identical. In contrast to Fig. 4, where proton transfer is triggered by a HOMO to LUMO transition at time $t = 0$, here proton transfer is induced by an external pulse excitation of the molecule (both inside and outside the cavity) with the form $\mathbf{E}_{\text{ext}}(t) = E_0 \exp(-t^2/\sigma^2) \cos(\omega t) \mathbf{e}_y$. In these simulations, $\sigma = 9.7$ fs, $\omega = 3.611$ eV outside the cavity (corresponding to the $S_0 \rightarrow S_1$ transition frequency), and $\omega = 3.355$ eV inside the cavity (corresponding to the LP frequency). Moreover, $E_0 = 2 \times 10^{-2}$ a.u. for (c), 4×10^{-2} a.u. for (e), and 8×10^{-2} a.u. for (g). All other parameters are the same as in Fig. 4. The lineshapes of the external pulse in the frequency domain are plotted as yellow shaded curves together with the spectra in the upper panel. Inside the cavity, the pulse mainly excites the LP, and the cavity suppresses the proton transfer dynamics.

to Fig. 4, Fig. 5 shows the proton transfer dynamics for oHBA under a Gaussian pulse excitation with the form $\mathbf{E}_{\text{ext}}(t) = E_0 \exp(-t^2/\sigma^2) \cos(\omega t) \mathbf{e}_y$. The pulse width is set as $\sigma = 9.7$ fs. Outside the cavity, the pulse frequency is chosen to peak at the $S_0 \rightarrow S_1$ transition frequency ($\omega = 3.611$ eV), whereas inside the cavity, the pulse frequency is chosen to peak at the LP frequency ($\omega = 3.355$ eV). The yellow shaded curves in the upper panel depict the corresponding pulse lineshapes in the frequency domain. For Figs. 5(b)-(g), the geometry of the oHBA molecule is fixed to the same geometry used in Figs. 4(d,e) and the amplitude of the pulse is increased from $E_0 = 2 \times 10^{-2}$ a.u. (Fig. 5b,c) to 4×10^{-2} a.u. (Fig. 5d,e) to 8×10^{-2} a.u. (Fig. 5f,g). For all three pulse amplitudes, we observed a cavity suppression of proton transfer, in agreement with Fig. 4.

Our assumption that the pulse excites only the molecular subsystem (not the cavity mode) ensures similar initial conditions for the outside versus inside cavity situations, allowing a clean comparison between the inside versus outside cavity results. In reality, however, because plasmonic cavities usually have a much larger effective transition dipole moment than the confined molecule, the external pulse should interact more strongly with the cavity mode. Such a cavity enhancement of the external field amplitude should promote proton transfer, whereas the formation of polaritons, as we have observed in Fig. 4, is more likely to suppress proton transfer. These two effects clearly work against each other. Hence, in order to better simulate photoinduced proton transfer inside a plasmonic cavity, one should also take into account the cavity enhancement of the external field. Although our code can be easily extended to include this enhancement (i.e., by assigning a very large effective transition dipole moment to the cavity mode), we do not report such a simulation here as it is beyond the scope of this work.

5. Conclusion

In this manuscript, we have introduced the semiclassical RT-NEO-TDDFT approach for studying the real-time dynamics of molecular polaritons. By treating electrons and specified nuclei quantum mechanically with RT-NEO-TDDFT and propagating the coupled dynamics between the quantum molecular subsystem and the classical cavity mode(s) self-consistently, this approach not only provides a unified description of ESC and VSC, but also can be used to probe the cavity effect on the coupled nuclear-electronic dynamics. Our application of this approach to excited state intramolecular proton transfer under single-molecule strong coupling is generally consistent with the previous work⁸³ showing that ESC can lead to suppression of photochemical reactions. However, our work reveals a new consideration for the investigation of cavity effects on chemical reactions: under single-molecule strong coupling for only the reactant, the cavity does not play a significant role when the chemical reaction timescale is faster than the Rabi oscillation timescale. In this case, the chemical reaction itself provides a strong lossy channel that may destroy strong coupling. As these timescales cannot be directly observed from the polaritonic potential energy surfaces, this work also highlights the importance of propagating real-time dynamics instead of considering only energetics. Furthermore, this semiclassical approach provides the foundation for exploring collective strong coupling in chemical systems within optical cavities.

Supporting information

Q-Chem input files and molecular geometries for the reported results; figure of the polariton spectrum for a single HCN molecule under ESC when the light-matter coupling strength or the cavity loss rate is tuned; figures of the proton transfer dynamics with a large Rabi splitting or with a cavity loss lifetime of 10 fs. The input files and plotting scripts are also available at Github (<https://github.com/TaoELi/semiclassical-rt-neo>).

Acknowledgement

This material is based upon work supported by the Air Force Office of Scientific Research under AFOSR Award No. FA9550-18-1-0134. We thank John Tully, Alexander Soudakov, Jonathan Fetherolf, Qi Yu, Chris Malbon, and Mathew Chow for useful discussions.

References

- (1) Ribeiro, R. F.; Martínez-Martínez, L. A.; Du, M.; Campos-Gonzalez-Angulo, J.; Yuen-Zhou, J. Polariton Chemistry: Controlling Molecular Dynamics with Optical Cavities. *Chem. Sci.* **2018**, *9*, 6325–6339.
- (2) Flick, J.; Narang, P. Cavity-Correlated Electron-Nuclear Dynamics from First Principles. *Phys. Rev. Lett.* **2018**, *121*, 113002.
- (3) Herrera, F.; Owrutsky, J. Molecular Polaritons for Controlling Chemistry with Quantum Optics. *J. Chem. Phys.* **2020**, *152*, 100902.
- (4) Xiang, B.; Xiong, W. Molecular Vibrational Polariton: Its Dynamics and Potentials in Novel Chemistry and Quantum Technology. *J. Chem. Phys.* **2021**, *155*, 050901.
- (5) Garcia-Vidal, F. J.; Ciuti, C.; Ebbesen, T. W. Manipulating Matter by Strong Coupling to Vacuum Fields. *Science* **2021**, *373*, eabd0336.
- (6) Li, T. E.; Cui, B.; Subotnik, J. E.; Nitzan, A. Molecular Polaritonics: Chemical Dynamics Under Strong Light–Matter Coupling. *Annu. Rev. Phys. Chem.* **2022**, *73*.
- (7) Coles, D. M.; Somaschi, N.; Michetti, P.; Clark, C.; Lagoudakis, P. G.; Savvidis, P. G.; Lidzey, D. G. Polariton-Mediated Energy Transfer between Organic Dyes in A Strongly Coupled Optical Microcavity. *Nat. Mater.* **2014**, *13*, 712–719.

- (8) Zhong, X.; Chervy, T.; Zhang, L.; Thomas, A.; George, J.; Genet, C.; Hutchison, J. A.; Ebbesen, T. W. Energy Transfer between Spatially Separated Entangled Molecules. *Angew. Chemie Int. Ed.* **2017**, *56*, 9034–9038.
- (9) Xiang, B.; Ribeiro, R. F.; Du, M.; Chen, L.; Yang, Z.; Wang, J.; Yuen-Zhou, J.; Xiong, W. Intermolecular Vibrational Energy Transfer Enabled by Microcavity Strong Light–Matter Coupling. *Science (80-.)*. **2020**, *368*, 665–667.
- (10) Orgiu, E.; George, J.; Hutchison, J. A.; Devaux, E.; Dayen, J. F.; Doudin, B.; Stellacci, F.; Genet, C.; Schachenmayer, J.; Genes, C.; Pupillo, G.; Samorì, P.; Ebbesen, T. W. Conductivity in Organic Semiconductors Hybridized with the Vacuum Field. *Nat. Mater.* **2015**, *14*, 1123–1129.
- (11) Hutchison, J. A.; Schwartz, T.; Genet, C.; Devaux, E.; Ebbesen, T. W. Modifying Chemical Landscapes by Coupling to Vacuum Fields. *Angew. Chemie* **2012**, *124*, 1624–1628.
- (12) Thomas, A.; George, J.; Shalabney, A.; Dryzhakov, M.; Varma, S. J.; Moran, J.; Chervy, T.; Zhong, X.; Devaux, E.; Genet, C.; Hutchison, J. A.; Ebbesen, T. W. Ground-State Chemical Reactivity under Vibrational Coupling to the Vacuum Electromagnetic Field. *Angew. Chemie Int. Ed.* **2016**, *55*, 11462–11466.
- (13) Thomas, A.; Lethuillier-Karl, L.; Nagarajan, K.; Vergauwe, R. M. A.; George, J.; Chervy, T.; Shalabney, A.; Devaux, E.; Genet, C.; Moran, J.; Ebbesen, T. W. Tilting a Ground-State Reactivity Landscape by Vibrational Strong Coupling. *Science* **2019**, *363*, 615–619.
- (14) Imperatore, M. V.; Asbury, J. B.; Giebink, N. C. Reproducibility of Cavity-Enhanced Chemical Reaction Rates in the Vibrational Strong Coupling Regime. *J. Chem. Phys.* **2021**, *154*, 191103.

- (15) Deng, H.; Haug, H.; Yamamoto, Y. Exciton-Polariton Bose–Einstein Condensation. *Rev. Mod. Phys.* **2010**, *82*, 1489–1537.
- (16) Pelton, M.; Storm, S. D.; Leng, H. Strong Coupling of Emitters to Single Plasmonic Nanoparticles: Exciton-Induced Transparency and Rabi Splitting. *Nanoscale* **2019**, *11*, 14540–14552.
- (17) Santhosh, K.; Bitton, O.; Chuntunov, L.; Haran, G. Vacuum Rabi Splitting in a Plasmonic Cavity at the Single Quantum Emitter Limit. *Nat. Commun.* **2016**, *7*, ncomms11823.
- (18) Keeling, J.; Kéna-Cohen, S. Bose–Einstein Condensation of Exciton-Polaritons in Organic Microcavities. *Annu. Rev. Phys. Chem.* **2020**, *71*, 435–459.
- (19) Long, J. P.; Simpkins, B. S. Coherent Coupling between a Molecular Vibration and Fabry–Perot Optical Cavity to Give Hybridized States in the Strong Coupling Limit. *ACS Photonics* **2015**, *2*, 130–136.
- (20) George, J.; Shalabney, A.; Hutchison, J. A.; Genet, C.; Ebbesen, T. W. Liquid-Phase Vibrational Strong Coupling. *J. Phys. Chem. Lett.* **2015**, *6*, 1027–1031.
- (21) Ruggenthaler, M.; Flick, J.; Pellegrini, C.; Appel, H.; Tokatly, I. V.; Rubio, A. Quantum-Electrodynamical Density-Functional Theory: Bridging Quantum Optics and Electronic-Structure Theory. *Phys. Rev. A* **2014**, *90*, 012508.
- (22) Flick, J.; Ruggenthaler, M.; Appel, H.; Rubio, A. Atoms and Molecules in Cavities, from Weak to Strong Coupling in Quantum-Electrodynamics (QED) Chemistry. *Proc. Natl. Acad. Sci.* **2017**, *114*, 3026–3034.
- (23) Haugland, T. S.; Ronca, E.; Kjønstad, E. F.; Rubio, A.; Koch, H. Coupled Cluster Theory for Molecular Polaritons: Changing Ground and Excited States. *Phys. Rev. X* **2020**, *10*, 041043.

- (24) Li, X.; Mandal, A.; Huo, P. Cavity Frequency-Dependent Theory for Vibrational Polariton Chemistry. *Nat. Commun.* **2021**, *12*, 1315.
- (25) Luk, H. L.; Feist, J.; Toppari, J. J.; Groenhof, G. Multiscale Molecular Dynamics Simulations of Polaritonic Chemistry. *J. Chem. Theory Comput.* **2017**, *13*, 4324–4335.
- (26) Li, T. E.; Subotnik, J. E.; Nitzan, A. Cavity Molecular Dynamics Simulations of Liquid Water under Vibrational Ultrastrong Coupling. *Proc. Natl. Acad. Sci.* **2020**, *117*, 18324–18331.
- (27) Triana, J. F.; Hernández, F. J.; Herrera, F. The Shape of the Electric Dipole Function Determines the Sub-picosecond Dynamics of Anharmonic Vibrational Polaritons. *J. Chem. Phys.* **2020**, *152*, 234111.
- (28) F. Ribeiro, R.; Dunkelberger, A. D.; Xiang, B.; Xiong, W.; Simpkins, B. S.; Owrutsky, J. C.; Yuen-Zhou, J. Theory for Nonlinear Spectroscopy of Vibrational Polaritons. *J. Phys. Chem. Lett.* **2018**, *9*, 3766–3771.
- (29) Fregoni, J.; Granucci, G.; Coccia, E.; Persico, M.; Corni, S. Manipulating Azobenzene Photoisomerization through Strong Light–Molecule Coupling. *Nat. Commun.* **2018**, *9*, 4688.
- (30) Climent, C.; Galego, J.; Garcia-Vidal, F. J.; Feist, J. Plasmonic Nanocavities Enable Self-Induced Electrostatic Catalysis. *Angew. Chemie Int. Ed.* **2019**, *58*, 8698–8702.
- (31) Feist, J.; Fernández-Domínguez, A. I.; García-Vidal, F. J. Macroscopic QED for Quantum Nanophotonics: Emitter-Centered Modes as A Minimal Basis for Multiemitter Problems. *Nanophoton.* **2020**, *10*, 477–489.
- (32) Hoffmann, N. M.; Lacombe, L.; Rubio, A.; Maitra, N. T. Effect of Many Modes on Self-Polarization and Photochemical Suppression in Cavities. *J. Chem. Phys.* **2020**, *153*, 104103.

- (33) Tichauer, R. H.; Feist, J.; Groenhof, G. Multi-scale Dynamics Simulations of Molecular Polaritons: The Effect of Multiple Cavity Modes on Polariton Relaxation. *J. Chem. Phys.* **2021**, *154*, 104112.
- (34) Yang, J.; Ou, Q.; Pei, Z.; Wang, H.; Weng, B.; Shuai, Z.; Mullen, K.; Shao, Y. Quantum-Electrodynamical Time-Dependent Density Functional Theory within Gaussian Atomic Basis. *J. Chem. Phys.* **2021**, *155*, 064107.
- (35) Jaynes, E.; Cummings, F. Comparison of Quantum and Semiclassical Radiation Theories with Application to the Beam Maser. *Proc. IEEE* **1963**, *51*, 89–109.
- (36) Tavis, M.; Cummings, F. W. Exact Solution for an N-Molecule—Radiation-Field Hamiltonian. *Phys. Rev.* **1968**, *170*, 379–384.
- (37) Tavis, M.; Cummings, F. W. Approximate Solutions for an N-Molecule-Radiation-Field Hamiltonian. *Phys. Rev.* **1969**, *188*, 692–695.
- (38) Schäfer, C.; Flick, J.; Ronca, E.; Narang, P.; Rubio, A. Shining Light on the Microscopic Resonant Mechanism Responsible for Cavity-Mediated Chemical Reactivity. *arXiv* **2021**, 2104.12429.
- (39) Marques, M.; Gross, E. Time-Dependent Density Functional Theory. *Annu. Rev. Phys. Chem.* **2004**, *55*, 427–455.
- (40) Li, T. E.; Nitzan, A.; Subotnik, J. E. Collective Vibrational Strong Coupling Effects on Molecular Vibrational Relaxation and Energy Transfer: Numerical Insights via Cavity Molecular Dynamics Simulations**. *Angew. Chemie Int. Ed.* **2021**, *60*, 15533–15540.
- (41) Rosenzweig, B.; Hoffmann, N. M.; Lacombe, L.; Maitra, N. T. Analysis of the Classical Trajectory Treatment of Photon Dynamics for Polaritonic Phenomena. *J. Chem. Phys.* **2022**, *156*, 054101.

- (42) Sukharev, M.; Nitzan, A. Optics of Exciton–Plasmon Nanomaterials. *J. Phys. Condens. Matter* **2017**, *29*, 443003.
- (43) Chen, H.-T.; Li, T. E.; Nitzan, A.; Subotnik, J. E. Predictive Semiclassical Model for Coherent and Incoherent Emission in the Strong Field Regime: The Mollow Triplet Revisited. *J. Phys. Chem. Lett.* **2019**, *10*, 1331–1336.
- (44) Chen, H.; McMahon, J. M.; Ratner, M. A.; Schatz, G. C. Classical Electrodynamics Coupled to Quantum Mechanics for Calculation of Molecular Optical Properties: a RT-TDDFT/FDTD Approach. *J. Phys. Chem. C* **2010**, *114*, 14384–14392.
- (45) Yamada, S.; Noda, M.; Nobusada, K.; Yabana, K. Time-Dependent Density Functional Theory for Interaction of Ultrashort Light Pulse with thin Materials. *Phys. Rev. B* **2018**, *98*, 245147.
- (46) Tancogne-Dejean, N. et al. Octopus, A Computational Framework for Exploring Light-Driven Phenomena and Quantum Dynamics in Extended and Finite Systems. *J. Chem. Phys.* **2020**, *152*, 124119.
- (47) Bustamante, C. M.; Gadea, E. D.; Horsfield, A.; Todorov, T. N.; González Lebrero, M. C.; Scherlis, D. A. Dissipative Equation of Motion for Electromagnetic Radiation in Quantum Dynamics. *Phys. Rev. Lett.* **2021**, *126*, 087401.
- (48) Schäfer, C.; Johansson, G. Efficient Self-Consistent Prediction of Natural Linewidths, Electromagnetically Induced Transparency, Superradiant and Purcell-Enhanced Emission for Realistic Materials using TDDFT. *arXiv* **2021**, 2109.09839.
- (49) Zhao, L.; Tao, Z.; Pavošević, F.; Wildman, A.; Hammes-Schiffer, S.; Li, X. Real-Time Time-Dependent Nuclear-Electronic Orbital Approach: Dynamics beyond the Born-Oppenheimer Approximation. *J. Phys. Chem. Lett.* **2020**, *11*, 4052–4058.

- (50) Li, T.-C.; Tong, P.-Q. Time-Dependent Density-Functional Theory for Multicomponent Systems. *Phys. Rev. A* **1986**, *34*, 529–532.
- (51) van Leeuwen, R.; Gross, E. K. U. In *Time-Dependent Density Functional Theory*; Marques, M. A., Ullrich, C. A., Nogueira, F., Rubio, A., Burke, K., Gross, E. K. U., Eds.; Springer Berlin Heidelberg, 2006; pp 93–106.
- (52) Butriy, O.; Ebadi, H.; de Boeij, P. L.; van Leeuwen, R.; Gross, E. K. U. Multicomponent Density-Functional Theory for Time-Dependent Systems. *Phys. Rev. A* **2007**, *76*, 052514.
- (53) Chakraborty, A.; Pak, M. V.; Hammes-Schiffer, S. Development of Electron-Proton Density Functionals for Multicomponent Density Functional Theory. *Phys. Rev. Lett.* **2008**, *101*, 153001.
- (54) Yang, Y.; Brorsen, K. R.; Culpitt, T.; Pak, M. V.; Hammes-Schiffer, S. Development of A Practical Multicomponent Density Functional for Electron-Proton Correlation to Produce Accurate Proton Densities. *J. Chem. Phys.* **2017**, *147*, 114113.
- (55) Brorsen, K. R.; Yang, Y.; Hammes-Schiffer, S. Multicomponent Density Functional Theory: Impact of Nuclear Quantum Effects on Proton Affinities and Geometries. *J. Phys. Chem. Lett.* **2017**, *8*, 3488–3493.
- (56) Pavošević, F.; Culpitt, T.; Hammes-Schiffer, S. Multicomponent Quantum Chemistry: Integrating Electronic and Nuclear Quantum Effects via the Nuclear–Electronic Orbital Method. *Chem. Rev.* **2020**, *120*, 4222–4253.
- (57) Yang, Y.; Culpitt, T.; Hammes-Schiffer, S. Multicomponent Time-Dependent Density Functional Theory: Proton and Electron Excitation Energies. *J. Phys. Chem. Lett.* **2018**, *9*, 1765–1770.

- (58) Culpitt, T.; Yang, Y.; Schneider, P. E.; Pavošević, F.; Hammes-Schiffer, S. Molecular Vibrational Frequencies with Multiple Quantum Protons within the Nuclear-Electronic Orbital Framework. *J. Chem. Theory Comput.* **2019**, *15*, 6840–6849.
- (59) Culpitt, T.; Yang, Y.; Pavošević, F.; Tao, Z.; Hammes-Schiffer, S. Enhancing the Applicability of Multicomponent Time-Dependent Density Functional Theory. *J. Chem. Phys.* **2019**, *150*, 201101.
- (60) Miller, W. H. The Semiclassical Initial Value Representation: A Potentially Practical Way for Adding Quantum Effects to Classical Molecular Dynamics Simulations. *J. Phys. Chem. A* **2001**, *105*, 2942–2955.
- (61) Cotton, S. J.; Miller, W. H. Symmetrical Windowing for Quantum States in Quasi-Classical Trajectory Simulations. *J. Phys. Chem. A* **2013**, *117*, 7190–7194.
- (62) Li, T. E.; Chen, H.-T.; Nitzan, A.; Subotnik, J. E. Quasiclassical Modeling of Cavity Quantum Electrodynamics. *Phys. Rev. A* **2020**, *101*, 033831.
- (63) Hoffmann, N. M.; Schäfer, C.; Säkkinen, N.; Rubio, A.; Appel, H.; Kelly, A. Benchmarking Semiclassical and Perturbative Methods for Real-Time Simulations of Cavity-Bound Emission and Interference. *J. Chem. Phys.* **2019**, *151*, 244113.
- (64) Cohen-Tannoudji, C.; Dupont-Roc, J.; Grynberg, G. *Photons and Atoms: Introduction to Quantum Electrodynamics*; Wiley: New York, 1997; pp 280–295.
- (65) Li, T. E.; Nitzan, A.; Subotnik, J. E. On the Origin of Ground-State Vacuum-Field Catalysis: Equilibrium Consideration. *J. Chem. Phys.* **2020**, *152*, 234107.
- (66) Schäfer, C.; Ruggenthaler, M.; Rokaj, V.; Rubio, A. Relevance of the Quadratic Diamagnetic and Self-Polarization Terms in Cavity Quantum Electrodynamics. *ACS Photonics* **2020**, *7*, 975–990.

- (67) Di Stefano, O.; Settineri, A.; Macrì, V.; Garziano, L.; Stassi, R.; Savasta, S.; Nori, F. Resolution of Gauge Ambiguities in Ultrastrong-Coupling Cavity Quantum Electrodynamics. *Nat. Phys.* **2019**, *15*, 803–808.
- (68) Li, T. E.; Chen, H.-T.; Nitzan, A.; Sukharev, M.; Subotnik, J. E. A Necessary Trade-off for Semiclassical Electrodynamics: Accurate Short-Range Coulomb Interactions versus the Enforcement of Causality? *J. Phys. Chem. Lett.* **2018**, 5955–5961.
- (69) Epifanovsky, E. et al. Software for the Frontiers of Quantum Chemistry: An Overview of Developments in the Q-Chem 5 Package. *J. Chem. Phys.* **2021**, *155*, 084801.
- (70) Goings, J. J.; Lestrangle, P. J.; Li, X. Real-Time Time-Dependent Electronic Structure Theory. *Wiley Interdiscip. Rev. Comput. Mol. Sci.* **2018**, *8*, e1341.
- (71) Li, X.; Smith, S. M.; Markevitch, A. N.; Romanov, D. A.; Levis, R. J.; Schlegel, H. B. A Time-Dependent Hartree–Fock Approach for Studying the Electronic Optical Response of Molecules in Intense Fields. *Phys. Chem. Chem. Phys.* **2005**, *7*, 233–239.
- (72) De Santis, M.; Storchi, L.; Belpassi, L.; Quiney, H. M.; Tarantelli, F. PyBERTHART: A Relativistic Real-Time Four-Component TDDFT Implementation Using Prototyping Techniques Based on Python. *J. Chem. Theory Comput.* **2020**, *16*, 2410–2429.
- (73) Mandal, A.; Montillo Vega, S.; Huo, P. Polarized Fock States and the Dynamical Casimir Effect in Molecular Cavity Quantum Electrodynamics. *J. Phys. Chem. Lett.* **2020**, *11*, 9215–9223.
- (74) Lee, C.; Yang, W.; Parr, R. G. Development of the Colle–Salvetti Correlation-Energy Formula into a Functional of the Electron Density. *Phys. Rev. B* **1988**, *37*, 785.
- (75) Becke, A. D. Density-Functional Exchange-Energy Approximation with Correct Asymptotic Behavior. *Phys. Rev. A* **1988**, *38*, 3098.

- (76) Becke, A. D. A New Inhomogeneity Parameter in Density-Functional Theory. *J. Chem. Phys.* **1998**, *109*, 2092.
- (77) Dunning, T. H. Gaussian Basis Sets for Use in Correlated Molecular Calculations. I. The Atoms Boron Through Neon and Hydrogen. *J. Chem. Phys.* **1989**, *90*, 1007–1023.
- (78) Bruner, A.; Lamaster, D.; Lopata, K. Accelerated Broadband Spectra Using Transition Dipole Decomposition and Padé Approximants. *J. Chem. Theory Comput.* **2016**, *12*, 3741–3750.
- (79) Pavošević, F.; Flick, J. Polaritonic Unitary Coupled Cluster for Quantum Computations. *J. Phys. Chem. Lett.* **2021**, *12*, 9100–9107.
- (80) Frisk Kockum, A.; Miranowicz, A.; De Liberato, S.; Savasta, S.; Nori, F. Ultrastrong coupling between light and matter. *Nat. Rev. Phys.* **2019**, *1*, 19–40.
- (81) Scheiner, S. Theoretical Studies of Excited State Proton Transfer in Small Model Systems. *J. Phys. Chem. A* **2000**, *104*, 5898–5909.
- (82) Aquino, A. J.; Lischka, H.; Hättig, C. Excited-State Intramolecular Proton Transfer: A Survey of TDDFT and RI-CC2 Excited-State Potential Energy Surfaces. *J. Phys. Chem. A* **2005**, *109*, 3201–3208.
- (83) Galego, J.; Garcia-Vidal, F. J.; Feist, J. Suppressing Photochemical Reactions with Quantized Light Fields. *Nat. Commun.* **2016**, *7*, 13841.

Supporting Information

Semiclassical Real-Time Nuclear-Electronic Orbital Dynamics for Molecular Polaritons: Unified Theory of Electronic and Vibrational Strong Couplings

Tao E. Li,* Zhen Tao, and Sharon Hammes-Schiffer*

Department of Chemistry, Yale University, New Haven, Connecticut, 06520, USA

E-mail: tao.li@yale.edu; sharon.hammes-schiffer@yale.edu

1. Q-Chem input file for HCN under VSC

HCN.in for Fig. 2c

```
$molecule
O 1
C 0.0 0.0 -0.5026771429
N 0.0 0.0 0.6555628571
H 0.0 0.0 -1.5728771429
$end

$rem
sym_ignore = 1
input_bohr = false
method = b3lyp
neo = true
neo_epc = epc172
basis = cc-pvdz
SCF_ALGORITHM = GDM
thresh = 14
s2thresh = 12
SCF_CONVERGENCE = 11
NEO_N_SCF_CONVERGENCE = 11
MAX_SCF_CYCLES = 500
NEO_PURECART = 1111
NEO_E_CONV = 12
MEM_TOTAL = 7000
NEO_VPP = 0
NEO_BASIS_LIN_DEP_THRESH = 8
$end

$neo_basis
H 3
```

S 1 1.000000
2.828400 1.0
S 1 1.000000
4.0 1.0
S 1 1.000000
5.6569 1.0
S 1 1.000000
8.0 1.0
S 1 1.000000
11.3137 1.0
S 1 1.000000
16.0 1.0
S 1 1.000000
22.6274 1.0
S 1 1.000000
32.0 1.0
P 1 1.000000
2.828400 1.0
P 1 1.000000
4.0 1.0
P 1 1.000000
5.6569 1.0
P 1 1.000000
8.0 1.0
P 1 1.000000
11.3137 1.0
P 1 1.000000
16.0 1.0
P 1 1.000000
22.6274 1.0
P 1 1.000000
32.0 1.0
D 1 1.000000

```

2.828400 1.0
D 1 1.000000
4.0 1.0
D 1 1.000000
5.6569 1.0
D 1 1.000000
8.0 1.0
D 1 1.000000
11.3137 1.0
D 1 1.000000
16.0 1.0
D 1 1.000000
22.6274 1.0
D 1 1.000000
32.0 1.0
$end

$neo_tdks
dt 0.04
maxiter 51677
field_type delta
field_amp 0.3
in_cavity true 0.3475 0 4e-4 1e8
rt_thresh 4
$end

```

The above input file can generate the data in Fig. 2c. The *\$neo_tdks* section controls the RT-NEO-TDDFT dynamics. While all of the other input parameters are self-explanatory, "*in_cavity true 0.3475 0 4e-4 1e8*" indicates coupling the molecule to a single-mode cavity with a frequency of 0.3475 a.u., polarization direction of x (0 to x , 1 to y , and 2 to z), coupling strength $\varepsilon = 4 \times 10^{-4}$ a.u., and lifetime $1/\gamma_c = 10^8$ a.u. Here, such a long lifetime

approximately means no cavity loss. "*rt_thresh 4*" indicates that the threshold of the predictor-corrector algorithm (the *eps* parameter in Algorithm 1 of Ref.^{S1}) is 10^{-4} .

2. Q-Chem input file for oHBA under ESC

oHBA.in for Fig. 4c

```
$molecule
O 1
C   -1.310008  1.258755  0.000000
C    0.019289  0.780580  0.000000
C    0.322586 -0.621636  0.000000
C   -0.761283 -1.465586  0.000000
C   -2.125342 -0.985468  0.000000
C   -2.398971  0.362640  0.000000
O    1.008708  1.658363  0.000000
C    1.725826 -1.062678  0.000000
O    2.682115 -0.219090  0.000000
H   -3.414260  0.733314  0.000000
H   -0.596742 -2.537818  0.000000
H   -2.926679 -1.713458  0.000000
H   -1.459388  2.331114  0.000000
H    1.924136 -2.138192  0.000000
H    1.844187  1.135044  0.000000
Gh   1.981048  0.913868  0.000000
Gh   2.117910  0.692694  0.000000
Gh   2.366459  0.659685  0.000000
$end

$rem
sym_ignore = 1
input_bohr = false
```

```
method = b3lyp
SCF_ALGORITHM = diis
MAX_SCF_CYCLES=200
basis = mixed
PURECART 1
SCF_CONVERGENCE = 8
mem_total = 7000
neo = true
NEO_E_CONV = 9
NEO_EPC = epc172
NEO_VPP = 0
$end
```

```
$basis
C 1
cc-pvdz
C 2
cc-pvdz
C 3
cc-pvdz
C 4
cc-pvdz
C 5
cc-pvdz
C 6
cc-pvdz
O 7
cc-pvdz
C 8
cc-pvdz
O 9
cc-pvdz
H 10
```

cc-pvdz

H 11

cc-pvdz

H 12

cc-pvdz

H 13

cc-pvdz

H 14

cc-pvdz

H 15

cc-pvdz

H 16

cc-pvdz

H 17

cc-pvdz

H 18

cc-pvdz

\$end

\$neo_basis

H 15

S 1 1.000000

4.0 1.0

P 1 1.000000

4.0 1.0

H 16

S 1 1.000000

4.0 1.0

P 1 1.000000

4.0 1.0

H 17

S 1 1.000000

4.0 1.0


```
P 1 1.000000
4.0 1.0
H 18
S 1 1.000000
4.0 1.0
P 1 1.000000
4.0 1.0
$end
```

```
$neo_tdks
electronic_HOMO2LUMO true
dt 0.04
maxiter 20000
field_type delta
field_amp 0e-2
in_cavity true 3.295 1 4e-3 1e8
rt_thresh 3
$end
```

The above input file can generate the data in Fig. 4c. In the *\$neo_tdks* section, "*electronic_HOMO2LUMO true*" enforces a HOMO to LUMO transition in the electronic density matrix at $t = 0$ (but by default this control is turned off).

The geometry of the oHBA molecule in Fig. 4e is

oHBA.xyz for Fig. 4e

```
C -1.301629 1.264863 0.000000
C 0.025677 0.802315 0.000000
C 0.308350 -0.595173 0.000000
C -0.771161 -1.469584 0.000000
C -2.105932 -1.005452 0.000000
```

```
C -2.364799  0.358631  0.000000
O  1.014139  1.694260  0.000000
C  1.693213 -1.060458  0.000000
O  2.668602 -0.278478  0.000000
H -3.383290  0.724581  0.000000
H -0.580558 -2.537265  0.000000
H -2.918862 -1.719777  0.000000
H -1.469874  2.334074  0.000000
H  1.853545 -2.147310  0.000000
H  1.860084  1.188551  0.000000
```

The additional three protonic basis function centers are the same as those in the above oHBA Q-Chem input file.

The geometry of the oHBA molecule in Fig. 4g is

oHBA.xyz for Fig. 4g

```
C -1.293251  1.270970  0.000000
C  0.032066  0.824049  0.000000
C  0.294115 -0.568710  0.000000
C -0.781038 -1.473582  0.000000
C -2.086523 -1.025436  0.000000
C -2.330627  0.354621  0.000000
O  1.019570  1.730158  0.000000
C  1.660600 -1.058238  0.000000
O  2.655089 -0.337865  0.000000
H -3.352319  0.715847  0.000000
H -0.564373 -2.536711  0.000000
H -2.911046 -1.726097  0.000000
H -1.480360  2.337034  0.000000
H  1.782954 -2.156428  0.000000
H  1.875980  1.242058  0.000000
```

The additional three protonic basis function centers are the same as those in the above oHBA Q-Chem input file.

For Fig. 5, in order to simulate proton transfer under an external Gaussian pulse excitation, we need to slightly change the *\$neo_tdks\$* input parameters:

\$neo_tdks\$ input parameters for Fig. 5

```
$neo_tdks
electronic_HOMO2LUMO false
dt 0.04
maxiter 20000
field_type gaussian 0.0 400.0 3.355
field_amp 8e-2
field_direction 1
in_cavity true 3.611 1 4e-3 1e8
in_cavity_excite_molecule true
rt_thresh 3
$end
```

Here, "*field_type gaussian 0.0 400.0 3.355*", "*field_amp 8e-2*", and "*field_direction 1*" collectively define an external Gaussian pulse with the following form: $\mathbf{E}_{\text{ext}}(t) = E_0 \exp[-(t-t_0)^2/\sigma^2] \cos(\omega t) \mathbf{e}_y$, where the field amplitude is $E_0 = 8 \times 10^{-2}$ a.u., $t_0 = 0$ a.u., $\sigma = 400.0$ a.u., and frequency $\omega = 3.355$ eV. Without the parameter "*field_direction 1*", the field will interact with the molecule in three dimensions. "*in_cavity_excite_molecule true*" ensures that the external pulse interacts only with the molecule (not the cavity mode). By default, the external field interacts with only the cavity mode.

3. Additional simulation data

3.1. Polaritonic spectra under ESC

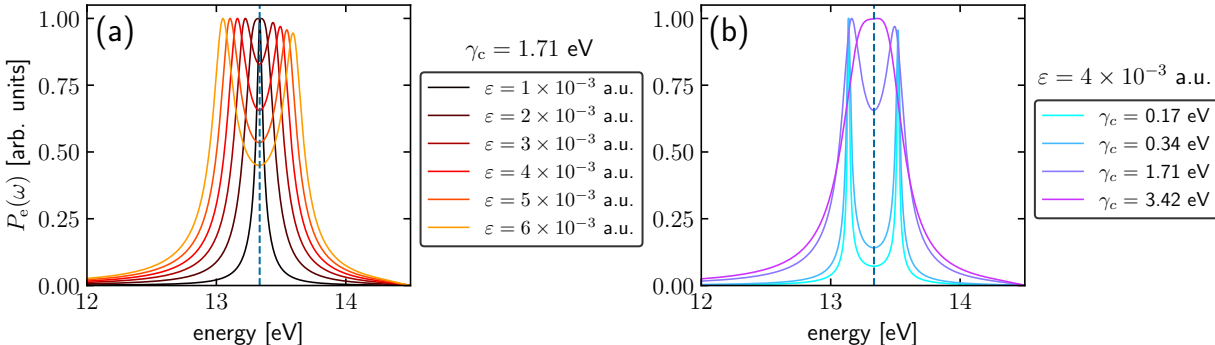


Figure S1: Power spectrum, $P_e(\omega)$, of the HCN electronic dipole moment when the HCN molecule is resonantly coupled to the z -polarized cavity with frequency $\omega_c = 13.334$ eV (vertical dashed blue lines). (a) The cavity loss is $\gamma_c = 1.71$ eV and the light-matter coupling strength ranges from $\varepsilon = 1 \times 10^{-3}$ a.u. (black line) to 6×10^{-3} a.u. (orange line). Note that a gradual increase of Rabi splitting is observed when the coupling strength is amplified. (b) The cavity loss ranges from $\gamma_c = 0.17$ eV (cyan line) to 3.42 eV (purple line) with the light-matter coupling strength set to $\varepsilon = 4 \times 10^{-3}$ a.u. Increasing the cavity loss transforms the system from strong coupling (with a peak splitting) to weak coupling (with no peak splitting). All other simulation details are the same as for Fig. 1d. Since the intrinsic molecular linewidth is 1.7×10^{-3} eV due to the small damping term $e^{-\gamma t}$ used for processing the real-time signals, all of the linewidths in this figure arise mainly from the coupling to the lossy cavity.

Fig. S1a demonstrates the electronic power spectrum inside a lossy cavity when the coupling strength is tuned from 1×10^{-3} a.u. (black line) to 6×10^{-3} a.u. (orange line) and all of the other simulation details are the same as in Fig. 1d. When the coupling strength is small ($\varepsilon \leq 2 \times 10^{-3}$ a.u.), since the cavity loss is large, the molecule is weakly coupled to the cavity mode and no peak splitting is observed. When the coupling strength increases, the Rabi splitting overcomes the cavity loss, and two polaritons are observed. Fig. S1b shows the effect of cavity loss on the molecular lineshape when the coupling strength is fixed as $\varepsilon = 4 \times 10^{-3}$ a.u. When the cavity loss increases from $\gamma_c = 0.17$ eV to 3.42 eV (cyan to purple), the peak splitting disappears.

3.2. Proton transfer under large light-matter coupling

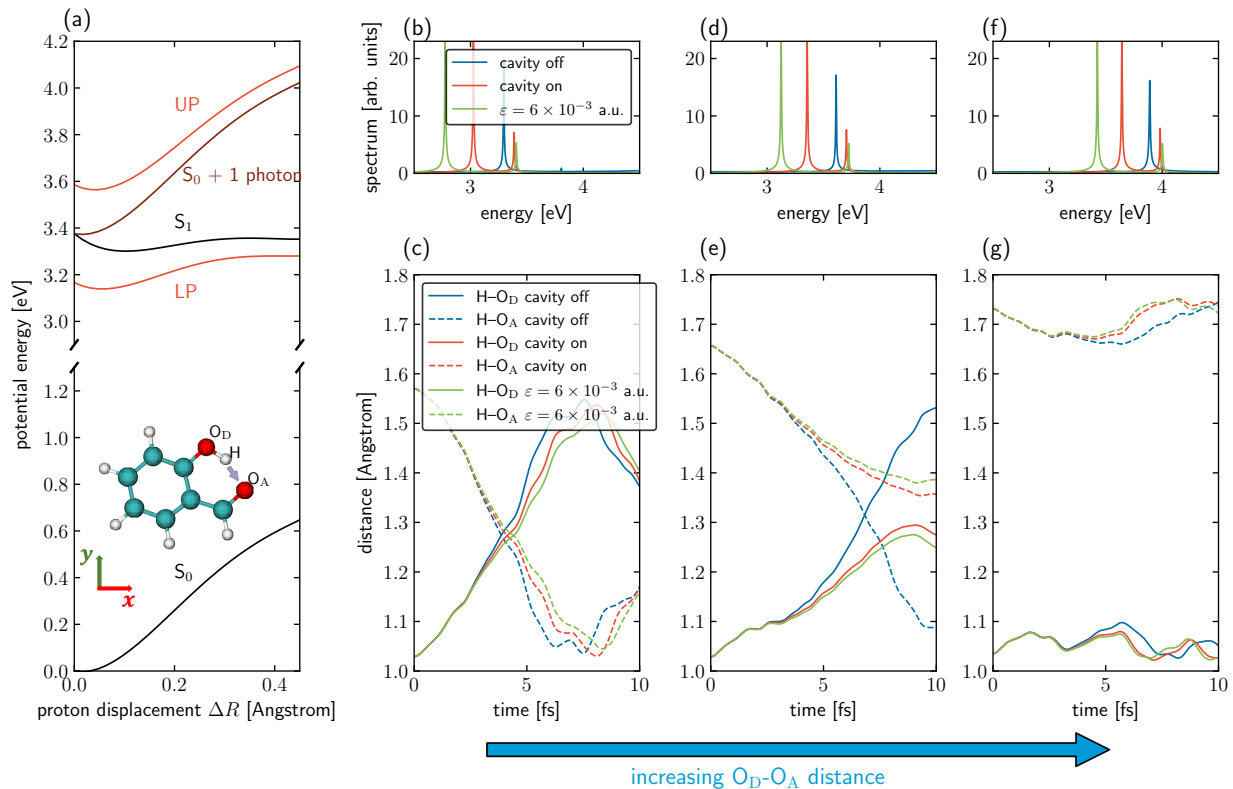


Figure S2: Another version of Fig. 4 in the main text. The only difference is that, from (b) to (g), the green lines represent the results corresponding to a large light-matter coupling $\epsilon = 6 \times 10^{-3}$ a.u., where all other parameters are the same as the inside cavity results in Fig. 4 obtained with $\epsilon = 4 \times 10^{-3}$ a.u. (red lines). Note that increasing the Rabi splitting can further suppress the proton transfer dynamics.

3.3. Proton transfer dynamics under a large cavity loss

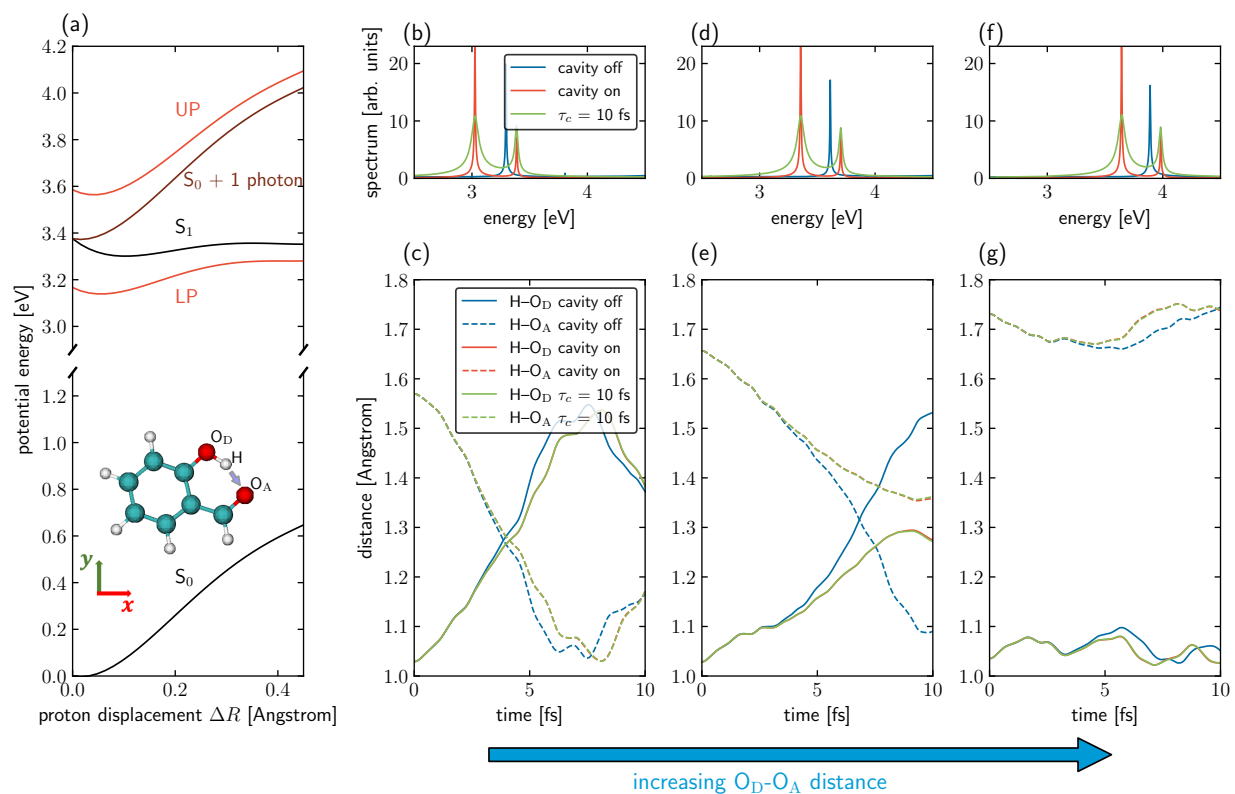


Figure S3: Another version of Fig. 4 in the main text. The only difference is that, from (b) to (g), the green lines represent the results corresponding to a large cavity loss $\tau_c = 1/\gamma_c = 10$ fs, where all other parameters are the same as the inside cavity results in Fig. 4 obtained with a lossless cavity (red lines). Note that adding a cavity loss broadens the polariton linewidths, but the proton transfer dynamics is not altered.

References

- [S1] De Santis, M.; Storchi, L.; Belpassi, L.; Quiney, H. M.; Tarantelli, F. PyBERTHART: A Relativistic Real-Time Four-Component TDDFT Implementation Using Prototyping Techniques Based on Python. *J. Chem. Theory Comput.* **2020**, *16*, 2410–2429.

Graphical TOC Entry

